Removal of core hole distortion from ionization edges in electron energy loss spectroscopy

B. G. Mendis[1] and Q. M. Ramasse[2,3]
[1]*Department of Physics, Durham University, South Road, Durham DH1 3LE, United Kingdom*
[2]*SuperSTEM, SciTech Daresbury Campus, Daresbury WA4 4AD, United Kingdom*
[3]*School of Chemical and Process Engineering and School of Physics and Astronomy, University of Leeds, Leeds LS2 9JT, United Kingdom*

(Received 15 February 2021; revised 12 April 2021; accepted 20 April 2021; published 3 May 2021)

The near-edge fine structure in electron energy loss spectra is used to probe the electronic bonding environment of materials at high spatial resolution. Often, however, deviations from the ground state electronic properties are observed, due to the core hole created within the ionized atom. A method is proposed to remove core hole distortion from experimental electron energy loss spectra by calculating the electrodynamic work done in separating the moving, incident electron from the oppositely charged core hole. Dynamic screening of the core hole is modeled using the material dielectric properties. The resulting energy gain spectrum is deconvolved from the experimental measurement to give a "fully screened" spectrum that is free of core hole distortion. The method is tested on core loss edges in elemental Si, SiC, and SiO_x. Despite assuming classical electrodynamics, the fundamental principle of an energy gain correction can be shown to be consistent with quantum mechanics, although shortcomings in some of the assumptions made on the nature of the core hole are also identified.

DOI: 10.1103/PhysRevB.103.205102

I. INTRODUCTION

In electron energy loss spectroscopy (EELS), and the similar technique of x-ray absorption spectroscopy, the fine structure observed in the core loss edge onset region is used to probe the local bonding environment of the ionized atom [1–4]. The fine structure should, in principle, yield information on the angular-momentum-resolved, unoccupied electronic density of states of the solid in the ground state. However, there is a substantial body of work (e.g., Refs. [5–9]) providing evidence to the contrary. The deviation from the ground state is due to the interaction between the atomic electron that is promoted to the conduction band and the partially screened charge of the atomic nucleus, i.e. the hole left behind in the core electronic level by the excited electron. This core hole interaction causes the final state wavefunction of the excited electron to be localized [10]; the stronger overlap between initial and final electronic states results in higher intensity at the edge threshold. If the binding energy of the core exciton is particularly strong, the edge onset may also be shifted to lower energy losses [11–13]. As a general rule, there is a direct correlation between the core hole interaction and degree of electronic screening within the material [14].

There are several approaches for including core hole interactions in EELS fine structure calculations, such as the two-body Bethe-Salpeter equation [15,16] and the computationally less expensive $Z+1$ approximation [5–9], where the ionized atom is replaced by the next element along the periodic table. Even for the latter the computation time is increased due to the need for a relatively large supercell that minimizes interaction between neighboring core holes, resulting from periodic boundary conditions in the simulation [17]. Since the strength of the core hole interaction depends on the level of screening, it is also not always clear if the $Z+1$ approximation is the best choice for a given material. For example, in MgO half-occupied Slater transition states have been found to provide a better match to experiment [18]. Therefore, what is desirable is a way to remove core hole effects from experimental EELS spectra. This would then enable interpretation of EELS data via the ground state properties of the solid, which can be calculated using, for example, density functional theory (DFT) methods.

In this paper, a straightforward method to remove core hole effects from EELS spectra is proposed. We calculate the energy gain of the incident electron along its trajectory due to Coulomb attraction with the core hole, which is dynamically screened by the electron "gas" in the solid. The dielectric function for the material is used to calculate screening. Strictly speaking, the energy gain here is smaller than the ionization loss and should therefore be interpreted as a "correction" to the overall EELS energy loss fine structure, rather than a directly measurable phenomenon, such as, for example, phonon energy gain spectroscopy [19] or the photon-induced near-field electron microscopy (PINEM) effect [20]. An energy gain spectrum can be derived based on the impact parameter distribution for the incident electron, which is governed by the illumination and detection conditions for the measurement. Deconvolving the energy gain spectrum from the experimental EELS spectrum gives a result that is more representative of the ground state. The advantage of this method is that it is easy to implement, with the deconvolved EELS spectrum being more amenable to simulation using electronic structure methods. The energy gain spectrum can also be used to gauge the strength of the core hole interaction, either in terms of screening within the bulk material or reduced screening within confined volumes or surfaces [21–24]. The mathemat-

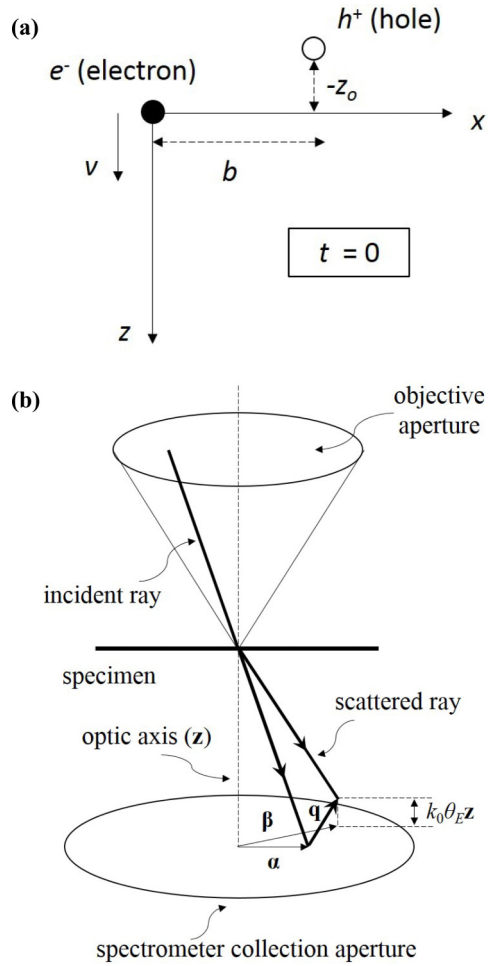

FIG. 1. (a) Schematic of inelastic scattering at the moment of core hole creation (time $t = 0$). The incident electron is traveling at speed v along the z axis with impact parameter b. The distance of separation between the electron and core hole along the z axis is z_0. (b) The scattering geometry for scanning transmission electron microscopy (STEM). An incident ray within the objective aperture has wavevector $\boldsymbol{\alpha}$ and is inelastically scattered to the wavevector $\boldsymbol{\beta}$ with scattering vector $\mathbf{q}$. Only scattered rays within the electron energy loss spectroscopy (EELS) spectrometer entrance aperture are detected.

ical details of the method and its comparison with quantum mechanics are presented in Secs. II and III, respectively, followed by application of the technique to experimental silicon L and K edges in elemental Si, hexagonal SiC, and amorphous SiO_x (Sec. V), which have varying degrees of screening as evidenced by their respective dielectric functions [25–27]. The limitations in the method are discussed in Sec. VI.

II. ENERGY GAIN SPECTRUM DUE TO CORE HOLE INTERACTION

Figure 1(a) is a schematic of the incident electron and ionized atom when the core hole is created at time $t = 0$. For simplicity, the ionized atomic electron is not considered; this omission is justified, since all the other electrons in the solid can effectively screen the core hole. The electron is traveling at speed v along the z axis with impact parameter b from the ionized atom measured along the x axis. The core hole is at a position $-z_0$ along the z axis when it first appears, i.e. z_0 is the distance the incident electron travels during the time it takes for the electronic transition to happen. By the uncertainty principle, z_0 is $\sim(v\hbar/\Delta E)$, where $\hbar$ is the reduced Planck constant and ΔE is the energy loss. It is assumed that the core hole interaction has a negligible effect on the trajectory and speed v of the swift electron; this will be discussed in more detail in Sec. III. Therefore, if $\phi(\mathbf{r},t)$ is the instantaneous electrostatic potential at position vector $\mathbf{r}$ due to the core hole, the work δW done over an infinitesimal path of the electron trajectory is given by the change in potential energy:

$$\delta W = -q_e\left[\frac{\partial\phi}{\partial t}\delta t + \frac{\partial\phi}{\partial z}\delta z\right] = -q_e\left[\frac{\partial\phi}{\partial t} + v\frac{\partial\phi}{\partial z}\right]\delta t, \quad (1)$$

with q_e being the electronic charge magnitude. It is convenient to express the potential as an inverse Fourier transform:

$$\phi(\mathbf{r},t) = \frac{1}{2\pi}\int \phi(\mathbf{q},\omega)\exp[2\pi i\mathbf{q}\cdot\mathbf{r} - i\omega t]d\mathbf{q}d\omega, \quad (2)$$

where $\mathbf{q}$ is a reciprocal vector, and ω is the angular frequency. Substituting in Eq. (1) and integrating δW over the entire electron trajectory (i.e. points $x, y = 0$ and $z = vt$), we obtain for the total work done

$$W(b) = -\frac{iq_e}{2\pi}\int_0^\infty \left\{\int (2\pi q_z v - \omega)\phi(\mathbf{q},\omega) \times \exp[i(2\pi q_z v - \omega)t]d\mathbf{q}d\omega\right\}dt, \quad (3)$$

Note that the infinite upper limit to the time integral effectively ignores the finite lifetime of the core hole, which can decay by Auger or radiative recombination [28]. This is justified since, for typical core hole lifetimes in EELS, the distance of separation between the core hole and incident electron is large enough to assume zero interaction. For instance, for a 0.015 eV (resp. 0.48 eV) lifetime broadening of the silicon L edge (resp. K edge) [28], a 60 kV incident electron would be 5878 nm (resp. 184 nm) away from the core hole when it decays. The time integral has the following solution:

$$\begin{aligned}\int_0^\infty &\exp[i(2\pi q_z v - \omega)t]dt \\ &= \int_{-\infty}^\infty H(t)\exp[i(2\pi q_z v - \omega)t]dt \\ &= \pi\delta(2\pi q_z v - \omega) + \frac{i}{(2\pi q_z v - \omega)}, \end{aligned} \quad (4)$$

where $H(t)$ is the Heaviside unit step function, and δ is the Dirac delta function. It then follows that

$$W(b) = \frac{q_e}{2\pi}\int \phi(\mathbf{q},\omega)d\mathbf{q}d\omega. \quad (5)$$

The core hole potential is obtained by Fourier transforming the Poisson equation [29]:

$$\phi(\mathbf{q},\omega) = \frac{\rho_f(\mathbf{q},\omega)}{4\pi^2 q^2\varepsilon_0\varepsilon(\mathbf{q},\omega)}. \quad (6)$$

Here, ε_0 is the permittivity of free space, $\varepsilon(\mathbf{q},\omega)$ is the dielectric function, and the free charge due to the core hole ρ_f is

given by $\rho_f(\mathbf{r},t) = q_e\delta(x-b)\delta(y)\delta(z+z_0)H(t)$; see Fig. 1(a). Therefore,

$$\rho_f(\mathbf{q},\omega) = \int \rho_f(\mathbf{r},t)\exp(-2\pi i\mathbf{q}\cdot\mathbf{r}+i\omega t)d\mathbf{r}dt$$
$$= q_e\exp(-2\pi iq_xb)\exp(2\pi iq_zz_0)\left[\pi\delta(\omega)+\frac{i}{\omega}\right], \quad (7)$$

where q_x and q_z are x, z components of $\mathbf{q}$, respectively. Substituting Eqs. (6) and (7) into Eq. (5) gives

$$W(b) = \frac{q_e^2}{8\pi^3\varepsilon_0}\int\frac{\exp(-2\pi iq_xb)\exp(2\pi iq_zz_0)}{q^2\varepsilon(\mathbf{q},\omega)} \times\left[\pi\delta(\omega)+\frac{i}{\omega}\right]d\mathbf{q}d\omega. \quad (8)$$

First consider the ω integral. Since $\varepsilon(\mathbf{r},t)$ is a real quantity, we have $\varepsilon(\mathbf{q},-\omega) = \varepsilon(\mathbf{q},\omega)^*$, where the asterisk denotes a complex conjugate. Therefore,

$$\int_{-\infty}^{\infty}\left[\pi\delta(\omega)+\frac{i}{\omega}\right]\frac{d\omega}{\varepsilon(\mathbf{q},\omega)}$$
$$= \int_{-\infty}^{0}\left[\pi\delta(\omega)+\frac{i}{\omega}\right]\frac{d\omega}{\varepsilon(\mathbf{q},\omega)}+\int_{0}^{\infty}\left[\pi\delta(\omega)+\frac{i}{\omega}\right]\frac{d\omega}{\varepsilon(\mathbf{q},\omega)}$$
$$= \int_{0}^{\infty}\left[\pi\delta(\omega)-\frac{i}{\omega}\right]\frac{d\omega}{\varepsilon(\mathbf{q},\omega)^*}+\int_{0}^{\infty}\left[\pi\delta(\omega)+\frac{i}{\omega}\right]\frac{d\omega}{\varepsilon(\mathbf{q},\omega)}$$
$$= 2\left\{\pi\mathrm{Re}\left[\frac{1}{\varepsilon(\mathbf{q},0)}\right]+\int_0^{\infty}\mathrm{Im}\left[\frac{-1}{\varepsilon(\mathbf{q},\omega)}\right]\frac{d\omega}{\omega}\right\}, \quad (9)$$

where Re and Im denote the real and imaginary part of a complex number. Substituting in Eq. (8) gives

$$W(b) = \frac{q_e^2}{4\pi^3\varepsilon_0}\left\{\pi\int\frac{\exp(-2\pi iq_xb)\exp(2\pi iq_zz_0)}{q^2} \times\mathrm{Re}\left[\frac{1}{\varepsilon(\mathbf{q},0)}\right]d\mathbf{q}+\int\frac{\exp(-2\pi iq_xb)\exp(2\pi iq_zz_0)}{q^2\omega} \times\mathrm{Im}\left[\frac{-1}{\varepsilon(\mathbf{q},\omega)}\right]d\omega d\mathbf{q}\right\}, \quad (10)$$

where the ω integral is now evaluated from 0 to ∞. The first and second terms within the curly brackets are the static and dynamic contributions to the core hole interaction. The static term indicates that the energy gain correction is small for materials with a large refractive index, consistent with the trend of weaker core hole effects in the presence of increased screening [14]. The dynamic term consists of the loss function [1], $\mathrm{Im}[-1/\varepsilon(\mathbf{q},\omega)]$, divided by ω. It follows that low loss inelastic scattering events, such as plasmon excitations, could have an important effect on the dynamic screening and therefore core hole interaction. Next consider the local approximation, i.e. $\varepsilon(\mathbf{q},\omega)$ is independent of $\mathbf{q}$. The scattering vector can be expressed as $\mathbf{q} = (\mathbf{q}_\perp, q_z)$, where $\mathbf{q}_\perp$ is the transverse component and q_z the component along the optic z axis. The integral over q_z in Eq. (10) is [30]

$$\int\frac{\exp(2\pi iq_zz_0)}{q_z^2+q_\perp^2}dq_z$$
$$= \int_{-\infty}^{\infty}\frac{\cos(2\pi q_zz_0)}{q_z^2+q_\perp^2}dq_z = \frac{\pi}{q_\perp}\exp(-2\pi z_0q_\perp), \quad (11)$$

Furthermore, for an EELS spectrometer aperture centered on the optic axis, and expressing $\mathbf{q}_\perp$ in polar coordinates $(q_\perp, \alpha)$,

$$\int\exp(-2\pi iq_xb)\left[\frac{\pi}{q_\perp}\exp(-2\pi z_0q_\perp)\right]d\mathbf{q}_\perp$$
$$= \int\exp(-2\pi iq_\perp b\cos\alpha)\left[\frac{\pi}{q_\perp}\exp(-2\pi z_0q_\perp)\right]q_\perp dq_\perp d\alpha$$
$$= 2\pi^2\int J_0(2\pi q_\perp b)\exp(-2\pi z_0q_\perp)dq_\perp, \quad (12)$$

where J_0 is the zero-order Bessel function of the first kind. The energy gain in the local approximation is therefore

$$W(b) = \frac{q_e^2}{2\pi\varepsilon_0}\left\{\pi\mathrm{Re}\left[\frac{1}{\varepsilon(0)}\right]+\int\frac{1}{\omega}\mathrm{Im}\left[-\frac{1}{\varepsilon(\omega)}\right]d\omega\right\} \times\int J_0(2\pi q_\perp b)\exp(-2\pi z_0q_\perp)dq_\perp. \quad (13)$$

The maximum energy gain $W_{\max}$ is obtained for zero impact parameter ($b = 0$), when the Coulomb attraction is strongest. From Eq. (13),

$$W_{\max} = \frac{q_e^2}{4\pi^2\varepsilon_0z_0}\left\{\pi\mathrm{Re}\left[\frac{1}{\varepsilon(0)}\right]+\int\frac{1}{\omega}\mathrm{Im}\left[-\frac{1}{\varepsilon(\omega)}\right]d\omega\right\} \times[1-\exp(-2\pi q_{\mathrm{EELS}}z_0)], \quad (14)$$

with q_{EELS} denoting the maximum scattering vector magnitude imposed by the EELS spectrometer. Equation (14) is an upper limit to the core hole interaction energy. For a very large EELS collection angle and a nonabsorptive medium {i.e. $\mathrm{Im}[\varepsilon(\omega)] = 0$}, Eq. (14) gives a $W_{\max}$ value of ${q_e}^2/(4\pi\varepsilon_0\varepsilon_rz_0)$, which is in agreement with the classical screened Coulomb potential energy (ε_r is the relative permittivity).

Thus far, we have only considered a single impact parameter b, although in an EELS experiment, there will be a range of impact parameter values depending on the illumination and detection conditions. For focused probe illumination in scanning transmission electron microscopy (STEM), the impact parameter distribution $P(b)$ for a single atom in free space is given by [31,32]

$$P(b)\propto\int A(\boldsymbol{\alpha})A(\boldsymbol{\alpha}')D(\boldsymbol{\beta})\exp\{i[\chi(\boldsymbol{\alpha}')-\chi(\boldsymbol{\alpha})]\} \times\exp[2\pi i\mathbf{b}\cdot(\boldsymbol{\alpha}'-\boldsymbol{\alpha})]\frac{S(\mathbf{q},\mathbf{q}',\Delta E)}{q^2q'^2}d^2\boldsymbol{\alpha}d^2\boldsymbol{\alpha}'d^2\boldsymbol{\beta}, \quad (15)$$

where χ is the lens aberration function, and $S(\mathbf{q},\mathbf{q}',\Delta E)$ is the dynamic form factor. Here, $\boldsymbol{\alpha}$, $\boldsymbol{\alpha}'$ represent any two transverse STEM probe wavevectors, and $\boldsymbol{\beta}$ is an EELS spectrometer entrance aperture wavevector [Fig. 1(b)]. The aperture functions for the STEM probe and EELS spectrometer are $A(\boldsymbol{\alpha})$ and $D(\boldsymbol{\beta})$. In the small angle, small energy loss limit the scattering vector $\mathbf{q}$ is given by $[k_0\theta_E\mathbf{z}+(\boldsymbol{\beta}–\boldsymbol{\alpha})]$, where k_0 is the wavenumber of the incident electrons of primary energy E_0, θ_E is the characteristic scattering angle ($=\Delta E/2E_0$), and $\mathbf{z}$ is a unit vector along the optic axis [1]. A similar expression is valid for the scattering vector $\mathbf{q}'$, but with $\boldsymbol{\alpha}'$ replacing $\boldsymbol{\alpha}$. Furthermore, in the dipole limit, the dynamic form factor is proportional to $\mathbf{q}\cdot\mathbf{q}'$ for nonmagnetic atoms [32].

It is now possible to calculate an energy gain spectrum due to the core hole interaction. For a given impact parameter, $W(b)$ determines the energy gain and $P(b)$ the intensity of the spectrum. For simplicity, we ignore the fact that many of the partial plane waves within a STEM probe are not fully parallel to the optic z axis, unlike the situation depicted in Fig. 1(a). The error this introduces is believed to be small for the mrad convergence semi-angles typical of STEM probes [33]. Deconvolving the energy gain spectrum from the background-subtracted, experimental EELS edge would yield a "fully screened" spectrum that is, in principle, free of core hole effects. Importantly, the fully screened spectrum is determined by the ground state properties of the solid and can therefore be directly calculated using electronic structure theory.

III. COMPARISON WITH QUANTUM MECHANICS

The previous section introduced an electrodynamic theory of scattering where the core hole interaction is modeled as an energy gain correction due to a change in potential energy. Here, it will be shown that this approach is consistent with quantum mechanics under certain conditions. According to the Ehrenfest theorem, the expectation value of an operator $\hat{Q}$ has the following time dependence [34]:

$$\frac{\partial\langle\hat{Q}\rangle}{\partial t} = \frac{i}{\hbar}\langle[\hat{H},\hat{Q}]\rangle + \left\langle\frac{\partial\hat{Q}}{\partial t}\right\rangle, \tag{16}$$

where $\hat{H}$ is the Hamiltonian, and the symbols [ ], < > denote the commutator and expectation value of operators, respectively. Consider the energy of the incident electron in a time-varying potential field $V(\mathbf{r},t)$, such as, for example, the field due to a dynamically screened core hole, which is suddenly created through inelastic scattering. Since the Hamiltonian $\hat{H} = \sum_j \frac{\hat{P}_j^2}{2m} - q_e V$, where $\hat{P}_j = -i\hbar\frac{\partial}{\partial x_j}$ is the momentum operator along the x_j Cartesian axis, the energy expectation value becomes

$$\frac{\partial\langle\hat{H}\rangle}{\partial t} = -q_e\left\langle\frac{\partial V(\mathbf{r},t)}{\partial t}\right\rangle. \tag{17}$$

Therefore, the energy of the incident electron is not fixed when the potential varies with time, unlike a closed system where energy is conserved due to the Hamiltonian being time independent. An example of a closed system would be an incident electron and a stationary positive charge in vacuum; as the electron moves away from the positive charge, the gain in potential energy is balanced by a loss in kinetic energy, such that the total energy is conserved. However, within a solid, the positive charge (i.e. the core hole) must first be created and is then screened by the background electron gas, resulting in an open system with time-dependent potential. A net energy change in the incident electron is therefore allowed.

From Eq. (16), we have

$$\frac{\partial\langle V\rangle}{\partial t} = \frac{i}{\hbar}\langle[\hat{H},V]\rangle + \left\langle\frac{\partial V}{\partial t}\right\rangle = \frac{i}{2m\hbar}\sum_j\langle[\hat{P}_j^2,V]\rangle + \left\langle\frac{\partial V}{\partial t}\right\rangle. \tag{18}$$

It is easy to show that $[\hat{P}_j,V] = \hat{P}_jV - V\hat{P}_j = -i\hbar\frac{\partial V}{\partial x_j}$, so that

$$[\hat{P}_j^2,V] = \hat{P}_j(\hat{P}_jV) - (V\hat{P}_j)\hat{P}_j = -i\hbar\left[\hat{P}_j\frac{\partial V}{\partial x_j} + \frac{\partial V}{\partial x_j}\hat{P}_j\right]. \tag{19}$$

The expectation value of the commutator is therefore

$$\langle[\hat{P}_j^2,V]\rangle = -\hbar^2\left[\left\langle\frac{\partial^2 V}{\partial x_j^2}\right\rangle + 2\left\langle\frac{\partial V}{\partial x_j}\frac{\partial}{\partial x_j}\right\rangle\right]. \tag{20}$$

Substituting in Eq. (18), we obtain

$$\frac{\partial\langle V\rangle}{\partial t} = -\frac{i\hbar}{2m}[\langle\nabla^2 V\rangle + 2\langle\vec{\nabla}V\cdot\vec{\nabla}\rangle] + \left\langle\frac{\partial V}{\partial t}\right\rangle. \tag{21}$$

Equation (17) then becomes

$$\frac{\partial\langle\hat{H}\rangle}{\partial t} = -q_e\left\{\frac{\partial\langle V\rangle}{\partial t} + \frac{i\hbar}{2m}[\langle\nabla^2 V\rangle + 2\langle\vec{\nabla}V\cdot\vec{\nabla}\rangle]\right\}. \tag{22}$$

The first term on the right-hand side is the time derivative of the potential energy expectation value. Since the Coulomb force $\mathbf{F}$ is proportional to $\vec{\nabla}V$, the second term can be interpreted as the divergence of the force (i.e. $\vec{\nabla}\cdot\mathbf{F}$), while the third term is attributed to the instantaneous power $\mathbf{F}\cdot\mathbf{v}$, where $\mathbf{v}$ is the incident electron velocity (this follows from the definition of the momentum operator $\hat{P} = -i\hbar\vec{\nabla}$ and the fact that momentum is proportional to the velocity). If the Coulomb force is small, the energy change is simply equal to the change in potential energy due to the time-dependent part of the potential, which is precisely what is calculated in Sec. II. Furthermore, the speed of the incident electron can also be treated as being constant, as was assumed in Eq. (1) (Sec. II). For the Coulomb force to be small the incident electron and core hole must be well separated, so that the method is only accurate for small energy losses, where z_0 is large and where delocalization gives rise to large impact parameters.

IV. EXPERIMENTAL METHODS

EELS spectra from [110]-Si, [11$\bar{2}$0]-SiC, and amorphous SiO_x (glass) were acquired using the Nion UltraSTEM 100 MC Hermes microscope at the SuperSTEM facility, Daresbury. The microscope operating voltage was 60 kV, and the energy resolution was set to 120 meV by adjusting the beam monochromator slit. Low loss and silicon L, K core loss edges were acquired at 0.05 eV/channel dispersion. The EELS spectrometer collection semi-angles were 18 and 36 mrad; for the Si K edge, however, only the larger collection angle was used due to the low count rate. The STEM probe semiconvergence angle was 31 mrad. EELS data were acquired by scanning the electron beam over a small area, typically a few nanometers in dimension, to minimize any electron beam damage as well as average over any potential sample inhomogeneities. For the crystalline samples, EELS spectra were acquired with the beam along the zone axis as well as the sample tilted off zone axis. Strictly speaking, Eq. (15) for the impact parameter distribution is valid for kinematic scattering and therefore cannot be applied to the zone axis data. However, the on-

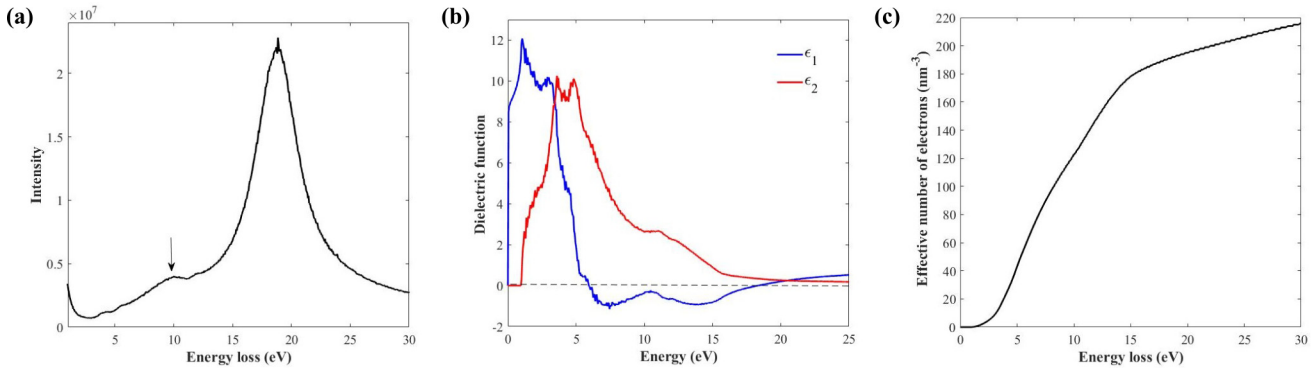

FIG. 2. (a) Low loss spectrum for elemental silicon showing a surface plasmon peak at 10 eV (arrowed feature). The Kramers-Kronig extracted dielectric function is shown in (b), with ε_1 and ε_2 being the real and imaginary parts, respectively. (c) The effective number of electrons as a function of energy loss.

and off-zone axis spectra were almost identical, and therefore, only the results for the former are presented.

The background under the core loss edges was subtracted using a power-law fit [1]. Furthermore, the long counting times for the Si K edge spectrum resulted in "spikes" due to stray x-rays, which were removed by replacing them with the average value of the counts on either side of the spike. The dielectric function was extracted from a Kramers-Kronig analysis of the low loss spectrum [1], with the data normalized using refractive index values of 3.5, 2.5, and 1.5 for Si, SiC, and SiO_x, respectively [25–27]. Before Kramers-Kronig analysis, the low loss spectrum was Fourier log deconvolved by fitting the zero-loss peak to a logarithmic function, as defined in the Gatan Digital Micrograph software. The Kramers-Kronig specimen thickness for elemental Si and SiC was in the region of 20–25 nm. The thin specimen, as well as the relatively low electron beam energy, reduces any Čerenkov radiation [35], although for core hole screening calculations, these artifacts should have a negligible effect, since Čerenkov losses are mainly present at energies close to the band gap where the EELS spectrum intensity is low [see Eq. (13)]. Since the specimens were thin, it was also assumed that the measured core loss spectra were largely free of multiple inelastic scattering. The amorphous SiO_x specimen thickness was, however, in the range of 55–70 nm, so that the core loss edges were Fourier log deconvolved before analysis.

V. RESULTS AND DISCUSSION

Results for elemental silicon will be discussed first. Figure 2(a) shows the silicon low loss spectrum acquired with an 18 mrad EELS spectrometer aperture and Fig. 2(b) the real (ε_1) and imaginary (ε_2) parts of the dielectric function extracted from a Kramers-Kronig analysis. The dielectric function was similar for both 18 and 36 mrad EELS spectrometer apertures, and therefore, only the results for the former are shown. The gross features of the EELS extracted dielectric function are similar to previous optical measurements [25], although the quantitative agreement is unsatisfactory. This could be due to the contribution of larger scattering angles in the EELS data, as well as the presence of residual surface losses, as evidenced by the surface plasmon loss peak at 10 eV in Fig. 2(a) [25]. Although the Kramers-Kronig analysis considered surface losses, some contribution remained, judging by the shape of the ε_1 curve. Furthermore, it is highly likely the silicon had a thin, native surface oxide layer. The surface quality of silicon is known to have an important effect on dielectric property measurement using spectroscopic ellipsometry [36] and may similarly influence EELS measurements as well. The effective number of electrons as a function of energy loss is shown in Fig. 2(c) and is in reasonable agreement with the theoretical value of 203 valence electrons/nm^3 at energy losses slightly above the bulk plasmon peak at 19 eV [Fig. 2(a)].

Using the EELS dielectric function, it is possible to calculate the energy gain spectrum for the experimental conditions. From Eq. (14), the maximum energy gain $W_{\max}$ is 0.92 eV for the silicon L edge and 18 mrad EELS spectrometer aperture. Only 0.19 eV is due to the static Coulomb interaction [first term in Eq. (14)], while most of the energy gain is due to incomplete dynamic screening. Figure 3(a) plots the dynamic contribution [second term in Eq. (14)] as a function of energy loss and indicates that the largest energy gain correction occurs at the bulk plasmon frequency, with lower frequencies above the band gap also contributing. In fact, from Eq. (14), any inelastic scattering mechanism at energy $\hbar\omega$ will give rise to an energy gain, the magnitude of which is inversely proportional to the frequency ω. In the case of collective excitations, such as a bulk plasmon, this has a relatively simple explanation. Plasmon oscillations in the electron density give rise to alternatingly higher and lower screening of the core hole charge, provided the separation between the incident electron and core hole is less than the plasmon wavelength. If the plasmon frequency is large, the rapid changes in the electron density will average out any fluctuations in the screening over the incident electron trajectory, so that there will only be a small contribution to the dynamic energy gain. Similar mechanisms may be responsible for the energy gain from single electron excitations. For example, resonance of the electron gas occurs at well-defined natural frequencies of the solid. Outside these natural frequencies, any oscillations in the electron gas will rapidly be dampened, so that the screening is like the static case.

The impact parameter distribution $P(b)$ in Eq. (15) is also important for the energy gain spectrum. Figure 3(b) shows $P(b)$ for the silicon L edge at 18 and 36 mrad EELS

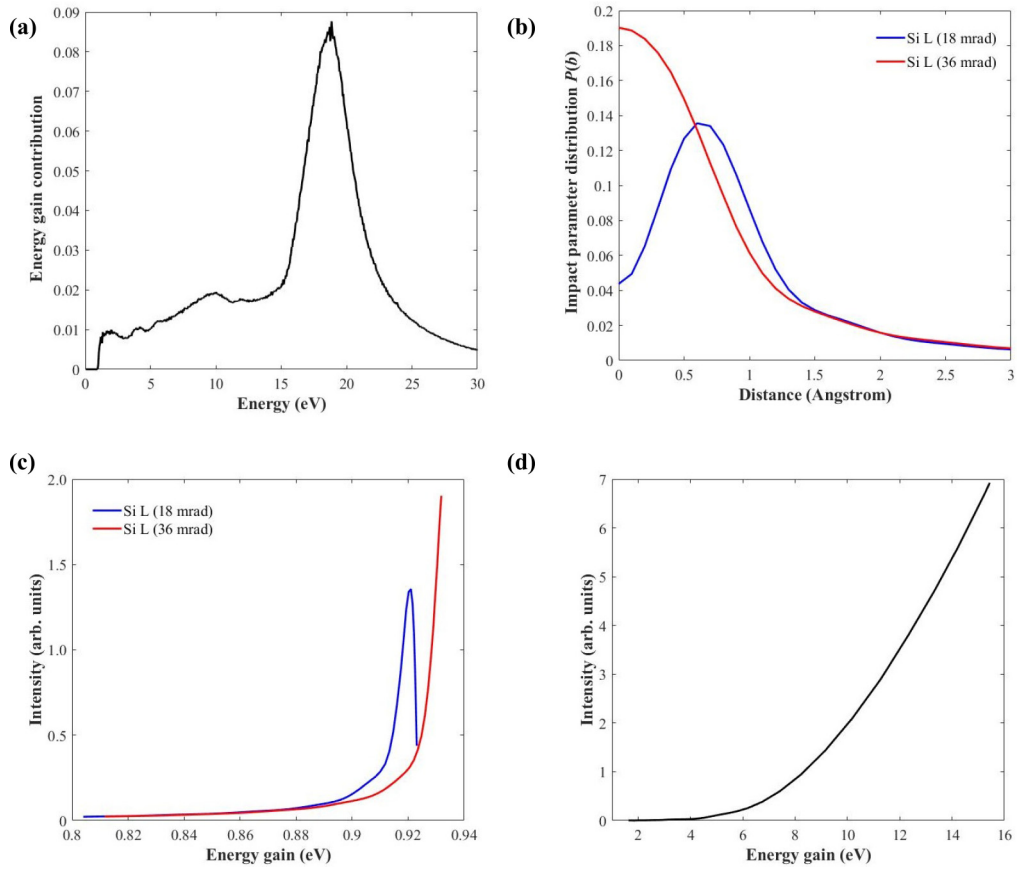

FIG. 3. (a) Dynamic contribution [i.e. second term in Eq. (14)] to the energy gain for the Si L ionization event at zero impact parameter in elemental silicon. The energy of the incident electron beam is 60 keV. The Si L edge impact parameter distributions $P(b)$ for a 60 kV, 31 mrad, aberration-free scanning transmission electron microscopy (STEM) probe and 18, 36 mrad electron energy loss spectroscopy (EELS) collection semi-angles are shown in (b), with (c) being the corresponding energy gain spectra. (d) The energy gain spectrum for the Si K edge at 36 mrad EELS semi-angle.

collection semi-angles (the STEM probe convergence semi-angle is 31 mrad, and all electron-optic aberrations are assumed to be zero). The former has a lower probability for ionization at small impact parameters, resulting in a "volcano" profile [37]. This is because small impact parameters result in larger scattering angles, as evidenced by $P(b)$ for the 36 mrad EELS aperture, which shows a monotonic decrease with impact parameter. $P(b)$ for the silicon L and K edges at 36 mrad EELS semi-angle and 31 mrad STEM probe semi-angle are found to have similar profiles. Figure 3(c) shows the energy gain spectra for Si L at 18 and 36 mrad EELS semi-angles calculated from the $P(b)$ profiles and Eq. (13). The former shows a sudden decrease in intensity at high energy losses due to the volcano profile of $P(b)$, but otherwise, the two spectra are similar and cover a narrow range in energy gain. On the other hand, the energy gain spectrum for the Si K edge at 36 mrad EELS collection semi-angle is much broader and has a maximum energy gain of 15.4 eV [Fig. 3(d)]. Although the $P(b)$ profiles for the Si L and K edges at 36 mrad EELS semi-angle are similar, there is a large difference in the minimum distance of separation [z_0; Fig. 1(a)] between the incident electron and core hole for the two ionization events. For example, at 60 keV beam energy, z_0 is 8.9 Å for Si L at 99 eV energy loss and 0.5 Å for Si K at 1839 eV energy loss. The smaller z_0 for the latter results in a larger energy gain due to an increased Coulomb interaction [Eq. (13)].

Figure 4(a) shows the measured 18 mrad EELS semi-angle, Si L edge in elemental silicon superimposed with the fully screened spectrum obtained after deconvolving the energy gain spectrum [Fig. 3(c)]. The edge onset for the fully screened spectrum is shifted to higher energy loss, consistent with previous observations from electronic structure theory that indicate core holes lead to stronger overlap between initial and final electronic states, thereby enhancing the intensity at the edge onset [10–13]. Although the fully screened spectrum is related to the measured spectrum by a convolution operation, the two spectra in Fig. 4(a) appear to be shifted with respect to one another by ∼1 eV. This is because the corresponding energy gain spectrum covers only a narrow energy range with a maximum energy of 0.92 eV; since it approximates to a delta function, convolution is similar to a shifting of the measured spectrum by the energy gain value. Duscher *et al.* [11] have performed pseudopotential electronic structure calculations of the Si L edge in elemental silicon with and without a core hole (the former using the $Z + 1$ approximation). The edge onset for the spectrum without a core hole is delayed by ∼0.5–1.0 eV, although there is no simple shifting of the two spectra, i.e. in addition to the delayed onset,

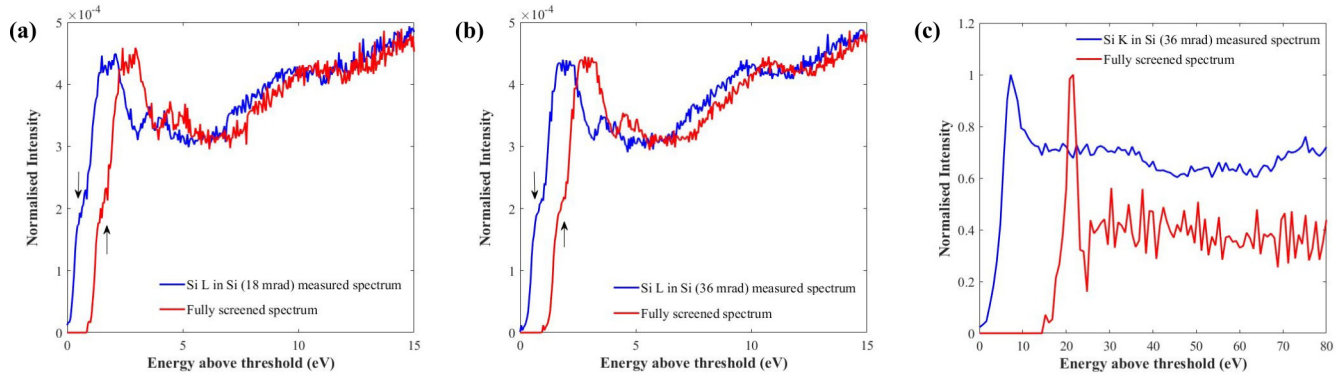

FIG. 4. Measured and fully screened Si L edges in elemental silicon are shown for (a) 18 mrad and (b) 36 mrad electron energy loss spectroscopy (EELS) collection semi-angles. The area of the two spectra in each plot are normalized for direct comparison. (c) The corresponding figure for the Si K edge in elemental silicon and 36 mrad EELS collection semi-angle. Here, the maximum intensity, rather than the area, is normalized due to the large energy shift between the measured and fully screened spectra.

there are also changes to the edge shape (see Fig. 1 of [11]). Although it is difficult to define a single value for the edge onset delay due to the change in edge shape, the estimated value for the electronic structure results in Ref. [11] is similar in magnitude to that obtained from our model. Close examination of Fig. 4(a) also reveals a small shoulder at the edge onset (feature marked by an arrow), which has been attributed to a core exciton [13,38]. Since this feature is due to the core hole interaction it should not be present in the fully screened spectrum, although this is clearly not the case in Fig. 4(a). By comparison, the core exciton feature is absent from electronic structure calculations performed without a core hole, but is otherwise observed in the $Z+1$ approximation [11]. This indicates that the calculated energy gain spectrum is not fully accurate; specifically, the energy gain peak should be broader than the width of the exciton peak (∼0.8 eV) to produce a noticeable change in edge shape during deconvolution, in addition to the energy shift observed in the present results.

The measured and fully screened Si L edge, 36 mrad EELS semi-angle spectra for pure silicon are shown in Fig. 4(b). The results are similar to Fig. 4(a), which is not surprising given the similarity in the energy gain spectra for the two experimental conditions [Fig. 3(c)]. Results for the Si K edge, 36 mrad EELS semi-angle data are presented in Fig. 4(c) and show large differences between the measured and fully screened spectra. Deconvolution of the energy gain spectrum from the measured spectrum resulted in amplification of any experimental noise; to minimize this artifact the measured spectrum had to be binned several times, so that the dispersion was reduced from 0.05 to 0.80 eV/channel. The edge onset for the fully screened spectrum is delayed by ∼14 eV [Fig. 4(c)]. In comparison, the edge onset delay is only ∼5 eV in Duscher *et al.* (see Fig. 6 in [11]). It should be noted that our model is not expected to give accurate results for high energy loss ionization events, such as the Si K edge. Apart from the arguments presented in Sec. III, the value of z_0 for the Si K edge is similar to the Bohr radius, so that it is doubtful if core hole screening can be accurately calculated using a continuum model.

The results for SiC will now be presented. Figure 5(a) shows the SiC dielectric function extracted from a low loss EELS spectrum acquired with 18 mrad collection semi-angle (the results for a 36 mrad spectrometer aperture were similar and are therefore not shown). The gross features are consistent with optical measurements [26], although there are differences in the numerical values for ε_1 and ε_2. Unlike elemental silicon, no surface plasmon peaks were observed for SiC, even though the Kramers-Kronig derived specimen thicknesses were similar for the two materials (i.e. 20–25 nm). The effective number of electrons plot is shown in Fig. 5(b). Hexagonal SiC has a valence electron density of 194 electrons/nm^3. This is considerably lower than the value of 294 electrons/nm^3 for 30 eV maximum energy loss, which includes the bulk plasmon peak, obtained from Fig. 5(b). Therefore, there are likely to be significant errors in the EELS extracted dielectric function.

The SiC energy gain spectra for the Si L edge at 18 and 36 mrad EELS collection semi-angles are shown in Fig. 5(c), while the Si K edge, 36 mrad EELS semi-angle energy gain spectrum is shown in Fig. 5(d). The energy gain for the Si L edge has a narrow distribution, with a maximum energy gain (1.00 eV) slightly higher than elemental silicon, due to SiC being more insulating. Consequently, the fully screened spectra for Si L at 18 and 36 mrad EELS semi-angles are largely energy shifted, with no significant change in edge shape compared with the measurement [Figs. 6(a) and 6(b)]. The energy shift is of a similar magnitude compared with the electronic structure calculations of Duscher *et al.* (see Fig. 9 in [11]). The fully screened spectrum for the Si K edge in SiC is shown in Fig. 6(c) (the measured spectrum was binned to a dispersion of 0.8 eV/channel to prevent any noise being amplified during deconvolution). Large changes in edge shape and onset are observed between the measurement and fully screened spectrum, due to the much broader energy range of the gain spectrum [Fig. 5(d)].

Figures 7(a) and 7(b) show the real and imaginary parts of the dielectric function for amorphous SiO_x, extracted from the 18 and 36 mrad collection semi-angle EELS spectra. The 18 mrad results are in good quantitative agreement with previous optical measurements (see Fig. 7 in Ref. [27]). The effective number of electrons as a function of energy loss is shown in Fig. 7(c). The valence electron density for crystalline α- and β-SiO_2 are 214 and 203 electrons/nm^3, respectively. The electron density for amorphous SiO_x will naturally be different to the crystalline forms, so that care must be taken

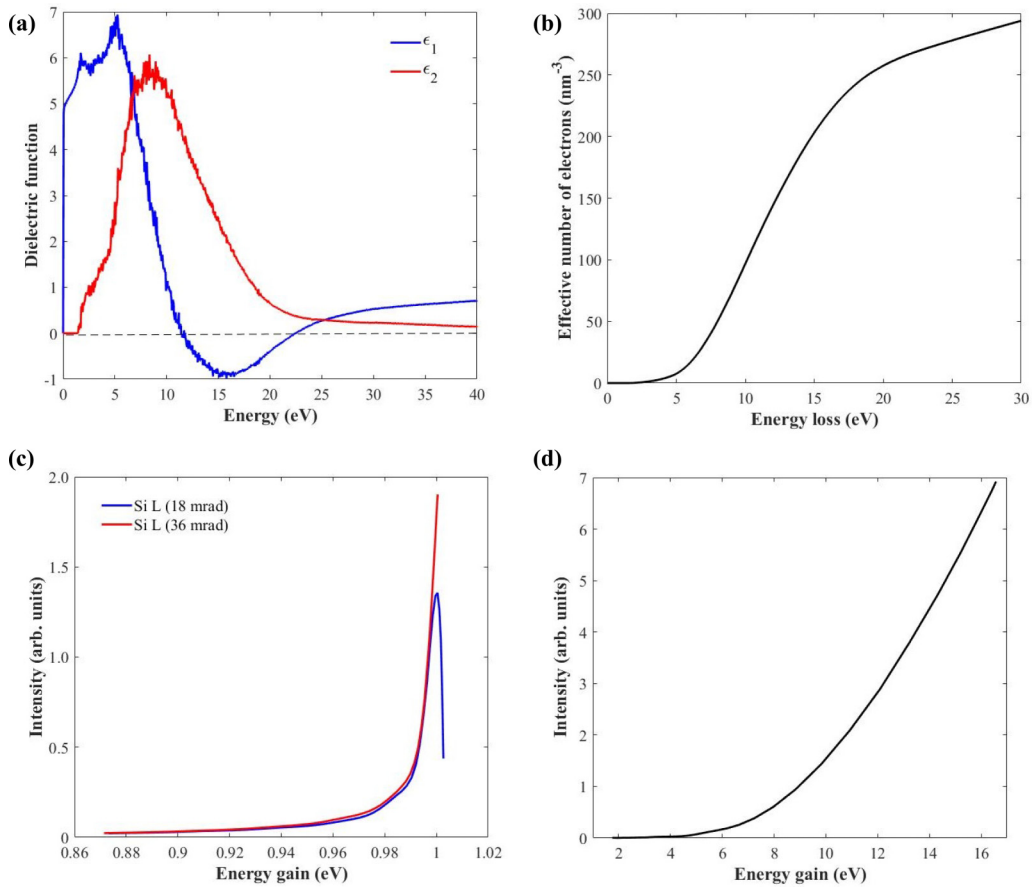

FIG. 5. (a) Kramers-Kronig extracted dielectric function for SiC and (b) the effective number of electrons as a function of energy loss. In (a) ε_1 and ε_2 are the real and imaginary parts of the dielectric function. Energy gain spectra for the Si *L* edge in SiC for 18 and 36 mrad electron energy loss spectroscopy (EELS) collection semi-angles are shown in (c). (d) The gain spectrum for the Si *K* edge in SiC at 36 mrad EELS semi-angle. The scanning transmission electron microscopy (STEM) probe parameters are 60 kV accelerating voltage, 31 mrad convergence semi-angle, and zero electron-optic aberrations.

in comparing experimental results with the calculated values. The high energy cutoff of the SiO_x plasmon is at ∼35 eV (full-width at half-maximum measure); from Fig. 7(c), the effective number of electrons for the 18 mrad results at 35 eV is 247 electrons/nm^3, which compares favorably with the calculated values, given the uncertainties noted above. The 18 mrad EELS dielectric function for amorphous SiO_x is therefore considered reasonably accurate. Unlike elemental Si and SiC, however, the dielectric function extracted from the 36 mrad EELS spectrum for amorphous SiO_x does not

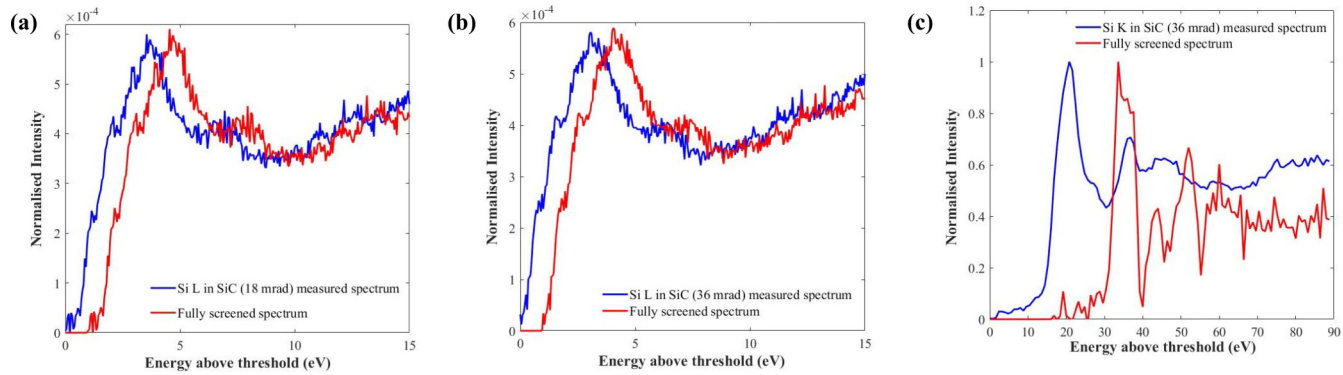

FIG. 6. Measured and fully screened Si *L* edges in SiC for (a) 18 mrad and (b) 36 mrad electron energy loss spectroscopy (EELS) collection semi-angles. The area of the two spectra in each plot are normalized for direct comparison. (c) The corresponding figure for the Si *K* edge in SiC at 36 mrad EELS collection semi-angle. Here, the maximum intensity, rather than the area, is normalized due to the large energy shift between the measured and fully screened spectra.

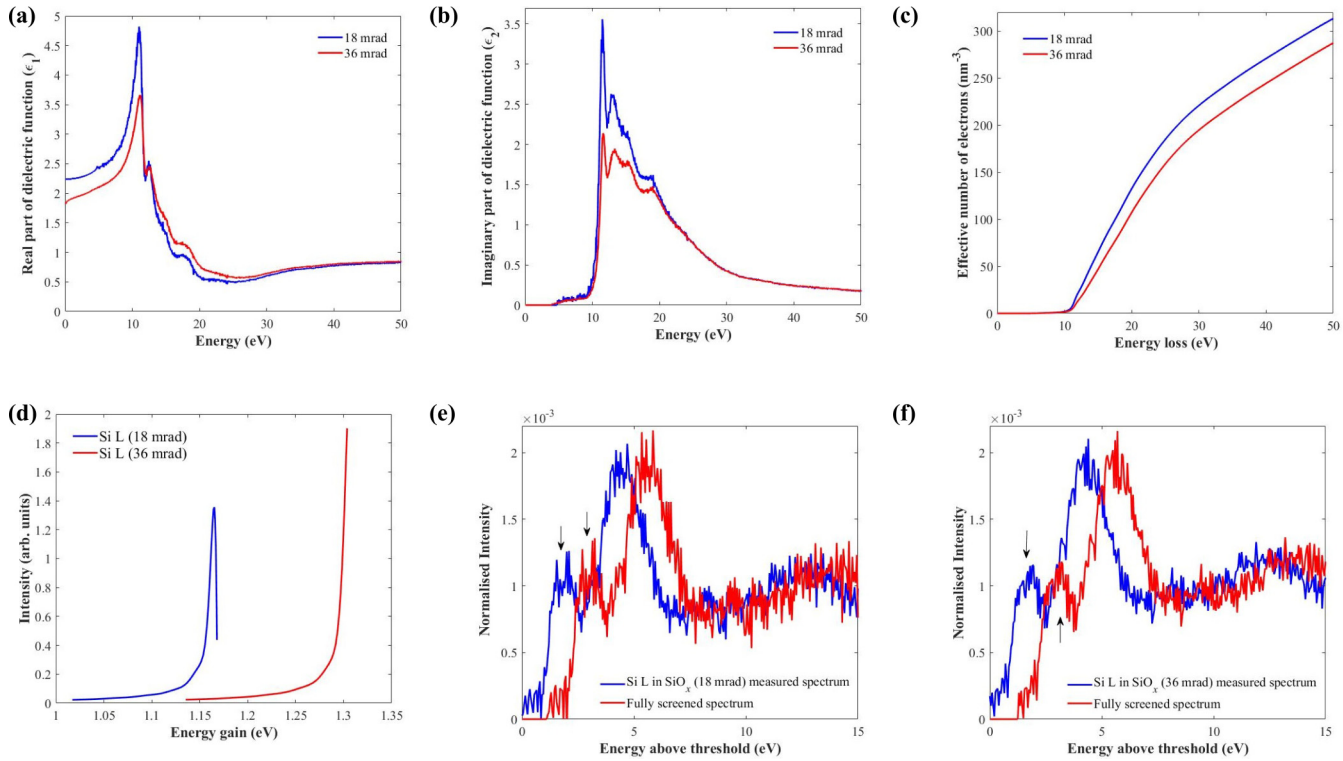

FIG. 7. (a) and (b) The real and imaginary parts of the dielectric function for amorphous SiO_x extracted from 18 and 36 mrad collection semi-angle electron energy loss spectroscopy (EELS) spectra. The effective number of electrons as a function of energy loss is shown in (c), while (d) plots the energy gain spectra for the Si L edge. The scanning transmission electron microscopy (STEM) probe parameters are 60 kV accelerating voltage, 31 mrad convergence semi-angle, and zero electron-optic aberrations. (e) and (f) The measured and fully screened Si L edges for 18 and 36 mrad EELS collection semi-angles, respectively. The area of the two spectra in each plot are normalized for direct comparison.

converge with the 18 mrad results, although the difference is small for most energies (the difference between $\varepsilon_1/\varepsilon_2$ for the two spectra was no more than 1.6).

Figure 7(d) shows the calculated energy gain spectra for the Si L edge in amorphous SiO_x for 18 and 36 mrad EELS collection semi-angles. Due to the insulating nature of SiO_x, the energy gain is slightly larger than elemental Si or SiC. Furthermore, the energy gain at 36 mrad is greater than at 18 mrad, which is due to the more localized inelastic scattering, as well as the slightly weaker static screening for the former (the static ε_1 value is 2.2 and 1.8 for the 18 and 36 mrad EELS spectra, respectively). The measured and fully screened Si L edge spectra at 18 and 36 mrad collection semi-angles are shown in Figs. 7(e) and 7(f), respectively. The core exciton feature (arrowed) is more prominent in amorphous SiO_x due to the reduced screening [38]. Furthermore, the core exciton has undergone doublet splitting, which is readily apparent in Fig. 7(e), the spacing between the doublet being ∼0.5 eV. A similar result was observed for α-SiO_2 using soft x-ray reflectivity measurements in a synchrotron [12], as well as EELS [38,39]. The doublet is due to excitons formed between the electron promoted to the 3s energy level and core hole in the 2p shell with $j = \frac{3}{2}$ and $\frac{1}{2}$ spin-orbit energies [12]. The higher energy resolution of monochromated STEM is critical for revealing fine structure in the excited state of the solid and produces results comparable with synchrotron x-rays, but with much better spatial resolution. However, as before, the core exciton is still visible in the fully screened spectrum, due to the narrow energy range in the gain spectrum largely giving rise to an energy shift during deconvolution with the experimental measurement. The generalized oscillator strength for a (ground state) silicon atom gives rise to a delayed maximum, partly due to the centrifugal barrier [40]. Although the bonding environment for silicon atoms in SiO_x is different to a free atom, the delayed maximum will tend to obscure any multiplet splitting; hence, a more featureless edge onset is expected for the fully screened Si L spectrum. The ∼1 eV shift in threshold energy for the fully screened spectrum is smaller than the ∼4–5 eV shift obtained from electronic structure simulations for crystalline quartz (see Fig. 3 in Ref. [11]). The maximum energy gain for the 36 mrad, Si K edge for amorphous SiO_x was 21.6 eV. With such a large energy gain, attempts to extract a fully screened spectrum for the Si K edge were unsuccessful; specifically, parts of the fully screened spectrum had negative intensity.

VI. LIMITATIONS OF THE MODEL

There are several limitations to the core hole model, which will now be discussed. Firstly, it is based on classical electrodynamics, and a comparison with quantum mechanics shows that this approach is only valid for small energy losses (Sec. III). Fully screened spectra for the Si K edge in elemental silicon and SiC appear to confirm this, since agreement

with the electronic structure calculations of Duscher *et al.* [11] is a lot worse than the lower energy Si L edge (Sec. V). The minimum separation z_0 between the incident electron and core hole is also only 0.5 Å for the Si K edge; it is therefore doubtful if continuum models of screening are applicable at these short length scales. Furthermore, we have not considered the plasmon wake trailing behind the incident electron [41]. The density oscillations in the electron gas due to the plasmon wake can potentially alter the core hole screening, especially for weakly bound core excitons [38].

However, the dominant error in the model appears to arise from the estimation of the z_0 parameter, i.e. the minimum separation between incident electron and core hole. Here, z_0 is estimated based on the energy-time form of the Heisenberg uncertainty relationship. The residual exciton peak apparent in the Si L edge fully screened spectrum indicates that the energy gain spectrum used for deconvolution is too narrow (Sec. V). This suggests that z_0 should be smaller than the current estimate. In fact, this can be justified using quantum mechanics as well. Consider a time-dependent Hamiltonian representing ionization of an atom, i.e. $H(\mathbf{r}_a, t) = H_o(\mathbf{r}_a) + H'(\mathbf{r}_a, t)$, where $H_o(\mathbf{r}_a)$ is the time-independent Hamiltonian, and $\mathbf{r}_a$ represents the position coordinates of the atomic electrons. The perturbation term $H'(\mathbf{r}_a, t) = q_e\mathbf{E}(\mathbf{r}_N, t)\cdot(\mathbf{r}_a - \mathbf{r}_N)$ is the potential energy of an electric dipole in the presence of an electric field $\mathbf{E}(\mathbf{r}_N, t)$ at the atom position $\mathbf{r}_N$. The electric field is due to the incident electron and is assumed to be approximately constant in the vicinity of the atom. If the initial state eigenfunction of the atom is $u_i(\mathbf{r}_a)$, then from time-dependent perturbation theory, the probability P_{fi} that the atom will be in the final state $u_f(\mathbf{r}_a)$ at time T is given by [34]

$$P_{\text{fi}}(T) = \left|\frac{1}{i\hbar}\int_0^T H'_{\text{fi}}(t)\exp(i\omega_{\text{fi}}t)dt\right|^2, \tag{23a}$$

$$H'_{\text{fi}}(t) = \int u_f(\mathbf{r}_a)^* H'(\mathbf{r}_a, t)u_i(\mathbf{r}_a)d\mathbf{r}_a, \tag{23b}$$

where $\hbar\omega_{\text{fi}} = E_f - E_i$ is the energy difference between the initial and final states. Derivation of Eq. (23a) assumes $u_f(\mathbf{r}_a)$ is an eigenfunction of $H_o(\mathbf{r}_a)$; this is not strictly true in the presence of a strong core hole, but let us ignore this subtlety for the moment. The electric field in the solid can be calculated using standard electrodynamic methods [42,43]. For an electron moving along the z axis with speed v, the charge density $\rho_f(\mathbf{r}, t) = -q_e\delta(x)\delta(y)\delta(z-vt)$, so that the Fourier transform of the electrostatic potential is

$$\phi(\mathbf{q}, \omega) = -\frac{q_e\delta(2\pi q_z v - \omega)}{4\pi^2 q^2\varepsilon_0\varepsilon(\mathbf{q}, \omega)}. \tag{24}$$

Inverse Fourier transforming the (non-retarded) electric field $\mathbf{E}(\mathbf{q}, \omega) = -2\pi i\mathbf{q}\phi(\mathbf{q}, \omega)$ gives

$$\mathbf{E}(\mathbf{r}_N, t) = \frac{iq_e}{8\pi^3 v\varepsilon_0}\int\frac{\mathbf{q}'\exp(2\pi i\mathbf{q}'\cdot\mathbf{r}_N)}{\varepsilon(\mathbf{q}', \omega)\left[q_\perp^2 + \left(\frac{\omega}{2\pi v}\right)^2\right]} \times \exp(-i\omega t)d\mathbf{q}_\perp d\omega, \tag{25}$$

where $\mathbf{q}' = (\mathbf{q}_\perp, q_z = \frac{\omega}{2\pi v})$. Substituting in Eqs. (23a) and (23b), the time integral has the form

$$\int_0^T \exp[i(\omega_{\text{fi}} - \omega)t]dt = \frac{\sin[(\omega_{\text{fi}} - \omega)T]}{(\omega_{\text{fi}} - \omega)} + i\frac{\sin^2[(\omega_{\text{fi}} - \omega)T/2]}{(\omega_{\text{fi}} - \omega)/2}. \tag{26}$$

For infinitely large T, the time integral has a pole at $\omega_{\text{fi}} = \omega$ [see Eq. (4)], consistent with the fact that energy must be conserved during ionization. However, for small T and $\omega_{\text{fi}} = \omega$, the time integral is equal to T, meaning that the atom has a non-zero probability of being ionized by the incident electron at distances smaller than the estimated value of z_0. To be consistent with quantum mechanics, we should therefore have a core hole charge that gradually builds up to its final value $+q_e$, rather than assuming a sudden appearance of the core hole in its final form at a fixed point in time. However, such a "partial" core hole is difficult to treat analytically and is also complicated by the fact that the transition probability [Eq. (23a)] assumes a final state eigenfunction that is unaffected by the core hole. The shape of the energy gain spectra in our calculations tend to mirror the electron impact parameter distribution of the measurement [see, for example, Fig. 3(a)]. However, the gain spectrum for a more complex partial core hole should contain additional fine structure that carries information on the time evolution of the core hole. This could potentially be explored through ultra-fast core loss spectroscopy, such as the work on graphite reported in Ref. [44], although in that study, the EELS fine structure was dominated by the lattice dynamics due to heating from the laser beam.

VII. SUMMARY

An electrodynamic model is proposed that, in principle, removes core hole distortion from electron energy loss spectra. An energy gain spectrum, based on the work done by the incident electron against the Coulomb attraction of the dynamically screened core hole, is calculated and deconvolved from the measured EELS spectrum. The resulting fully screened spectrum is easier to predict using electronic structure theory, since it only relies on the ground state properties of the solid. Quantum mechanics indicates that this classical approach is approximately valid for low energy loss ionization events. Application of the method to the Si L edge in elemental silicon, SiC, and amorphous SiO_x showed promising results, especially when compared with previous electronic structure calculations. However, residual core hole distortion remained, as evidenced by the fact that the core exciton feature in the Si L edge was not completely removed in the fully screened spectrum. Further analysis showed that this was due to assuming that the core hole appears suddenly at a fixed point in time, although quantum mechanically, there is a nonzero probability for the core hole to form at any point in time; effectively a partial core hole that over time develops into the final core hole configuration. Despite this limitation, the model is still useful for evaluating the effect of the core hole on an EELS edge shape. The fully screened spectrum is also better suited for electronic structure

calculations, which typically are only valid for the solid in its ground state. Recently, machine learning techniques, in the form of artificial neural networks, have been applied to predict excited state EELS spectra, starting from the ground state electronic density of states [45]. This approach can help identify key parameters influencing the excited state, such as, for example, the role of the material band gap on core hole screening in silicon oxides [45]. It may be possible to combine machine learning techniques with our method to explore, say, the role of plasmons and interband transitions on core hole screening for different classes of materials. Furthermore, the electrodynamic model can easily be adopted to more complex core hole screening geometries, such as free surfaces [21–24]. This will be the subject of a separate paper.

[1] R. F. Egerton, *Electron Energy-Loss Spectroscopy in the Electron Microscope* (Plenum Press, New York, 1996).

[2] D. A. Muller, T. Sorsch, S. Moccio, F. H. Baumann, K. Evans-Lutterodt, and G. Timp, Nature **399**, 758 (1999).

[3] Q. M. Ramasse, C. R. Seabourne, D. M. Kepaptsoglou, R. Zan, U. Bangert, and A. J. Scott, Nano Lett. **13**, 4989 (2013).

[4] B. G. Mendis, M. MacKenzie, and A. J. Craven, Ultramicroscopy **110**, 105 (2010).

[5] N. Jiang and J. C. H. Spence, Phys. Rev. B **69**, 115112 (2004).

[6] D. N. Jayawardane, C. J. Pickard, L. M. Brown, and M. C. Payne, Phys. Rev. B **64**, 115107 (2001).

[7] S. Nufer, T. Gemming, C. Elsässer, S. Küstlmeier, and M. Rühle, Ultramicroscopy **86**, 339 (2001).

[8] C. Elsässer and S. Küstlmeier, Ultramicroscopy **86**, 325 (2001).

[9] K. van Benthem, C. Elsässer, and M. Rühle, Ultramicroscopy **96**, 509 (2003).

[10] T. Mizoguchi, W. Olovsson, H. Ikeno, and I. Tanaka, Micron **41**, 695 (2010).

[11] G. Duscher, R. Buczko, S. J. Pennycook, and S. T. Pantelides, Ultramicroscopy **86**, 355 (2001).

[12] W. L. O'Brien, J. Jia, Q-Y. Dong, T. A. Callcott, J-E. Rubensson, D. L. Mueller, and D. L. Ederer, Phys. Rev. B **44**, 1013 (1991).

[13] M. Altarelli and D. L. Dexter, Phys. Rev. Lett. **29**, 1100 (1972).

[14] S-P. Gao, C. J. Pickard, M. C. Payne, J. Zhu, and J. Yuan, Phys. Rev. B **77**, 115122 (2008).

[15] E. L. Shirley, J. Electron Spectrosc. **144**, 1187 (2005).

[16] W. Olovsson, I. Tanaka, T. Mizoguchi, P. Pusching, and C. Ambrosch-Draxl, Phys. Rev. B **79**, 041102(R) (2009).

[17] C. R. Seabourne, A. J. Scott, R. Brydson, and R. J. Nicholls, Ultramicroscopy **109**, 1374 (2009).

[18] T. Mizoguchi, I. Tanaka, M. Yoshiya, F. Oba, K. Ogasawara, and H. Adachi, Phys. Rev. B **61**, 2180 (2000).

[19] M. J. Lagos and P. E. Batson, Nano Lett. **18** (2018) 4556.

[20] B. Barwick, D. J. Flannigan, and A. H. Zewail, Nature **462** (2009) 902.

[21] L. Siller, S. Krishnamurthy, L. Kjeldgaard, B. R. Horrocks, Y. Chao, A. Houlton, A.K. Chakraborty, and M. R. C. Hunt, J. Phys.: Condens. Matter **21**, 095005 (2009).

[22] G. J. Lapeyre and J. Anderson, Phys. Rev. Lett. **35**, 117 (1975).

[23] V. E. Henrich, G. Dresselhaus, and H. J. Zeiger, Phys. Rev. Lett. **36**, 158 (1976).

[24] M. Altarelli, G. Bachelet, and R. Del Sole, J. Appl. Phys. **16**, 1370 (1979).

[25] B. W. Reed, J. M. Chen, N. C. MacDonald, J. Silcox, and G. F. Bertsch, Phys. Rev. B **60**, 5641 (1999).

[26] J. Petalas, S. Logothetidis, M. Gioti, and C. Janowitz, Phys. Status Solidi B **209**, 499 (1998).

[27] G-L. Tan, M. F. Lemon, and R. H. French, J. Am. Ceram. Soc. **86**, 1885 (2003).

[28] J. C. Fuggle and J. E. Inglesfield, *Unoccupied Electronic States: Fundamentals for XANES, EELS, IPS and BIS* (Springer-Verlag, Berlin, 1992).

[29] N. W. Ashcroft and N. D. Mermin, *Solid State Physics* (Holt, Rinehart and Winston, 1976).

[30] I. S. Gradshteyn and I. M. Ryzhik, *Tables of Integrals, Series and Products* (Academic Press, New York, 1980).

[31] H. Kohl and H. Rose, Adv. Electron. Electron Phys. **65**, 173 (1985).

[32] D. A. Muller and J. Silcox, Ultramicroscopy **59**, 195 (1995).

[33] A. Howie and R. H. Milne, J. Microsc. **136**, 279 (1984).

[34] A. I. M. Rae, *Quantum Mechanics*, Fifth Edition (Taylor & Francis, New York, 2008).

[35] M. Stöger-Pollach, H. Franco, P. Schattschneider, S. Lazar, B. Schaffer, W. Grogger, and H. W. Zandbergen, Micron **37**, 396 (2006).

[36] D. E. Aspnes and A. A. Studna, Phys. Rev. B **27**, 985 (1983).

[37] E. C. Cosgriff, M. P. Oxley, L. J. Allen, and S. J. Pennycook, Ultramicroscopy **102**, 317 (2005).

[38] P. E. Batson, Phys. Rev. B **47**, 6898 (1993).

[39] O. L. Krivanek, T. C. Lovejoy, N. Dellby, and R. W. Carpenter, Microscopy **62**, 3 (2013).

[40] R. D. Leapman, P. Rez, and D. F. Mayers, J. Chem. Phys. **72**, 1232 (1980).

[41] P. M. Echenique, R. H. Ritchie, and W. Brandt, Phys. Rev. B **20**, 2567 (1979).

[42] R. H. Ritchie, Phys. Rev. **106**, 874 (1957).

[43] B. G. Mendis, *Electron Beam-Specimen Interactions and Simulation Methods in Microscopy* (Wiley, New Jersey, 2018).

[44] R. M. van der Veen, T. J. Penfold, and A. H. Zewail, Struct. Dyn. **2**, 024302 (2015).

[45] S. Kiyohara, M. Tsubaki, and T. Mizoguchi, npj Comput. Mater. **6**, 68 (2020).